*buildings*

MDPI

*Article*

# Spatiotemporal Characteristics of Street Canyon Microclimate: Insights from Cross-Seasonal Field Measurements and Coupled CFD Simulations

**Jiaqi Wang, Ye Min, Jing Tan and Zijing Tan ***

School of Civil Engineering, Chang'an University, Xi'an 710064, China; wangjiaqi@chd.edu.cn (J.W.); 2024228107@chd.edu.cn (Y.M.); 2022228111@chd.edu.cn (J.T.)
* Correspondence: tanzijing@chd.edu.cn

**Abstract**

Urban street canyons exert a critical influence on local microclimates; however, the dynamics of mixed convective airflow under unsteady wind and thermal forcing remain poorly quantified. This study systematically investigates the spatiotemporal characteristics of airflow within symmetric and asymmetric street canyons through integrated long-term field measurements and complementary CFD simulations. Field data collected over 120 monitoring days at the Weishui Campus of Chang'an University were analyzed using the Levenberg–Marquardt nonlinear curve-fitting algorithm. The analysis demonstrates that sine functions accurately represent diurnal surface temperature variations during consecutive clear sky periods, whereas polynomial functions of varying orders are required to characterize meteorologically complex episodes, including cold-wave cooling and seasonal transitions. Ambient wind patterns outside the canyon were further classified into two characteristic variation modes: stepwise and gradual. Complementary unsteady RANS simulations, with wall boundary conditions derived directly from the fitted field data, reveal that canyon geometry and meteorological forcing jointly govern the evolution of airflow structures and thermal distributions across seasons. In the symmetric canyon, the flow transitions from complex multi-vortex activity in spring and summer to a more stable regime in autumn, with two well-defined counter-rotating vortices emerging during winter cold-wave events. In the asymmetric canyon, strong summer solar heating sustains a dominant leeward vortex with a strengthening secondary structure, whereas winter cold wave intrusion generates a hierarchically nested vortex system in which secondary and tertiary vortices progressively develop and detach. By coupling empirical surface temperature functions with CFD boundary conditions, this study advances the precision of predictive microclimate models and provides an evidence-based framework for optimizing street canyon geometry to enhance ventilation performance, energy efficiency, and outdoor thermal comfort.

**Keywords:** wind environment; street canyon; field measurement; numerical simulation; surface temperature; cross-seasonal variation

Check for updates

Academic Editors: Derek Clements-Croome and Rafik Belarbi

Received: 11 March 2026
Revised: 8 May 2026
Accepted: 19 May 2026
Published: 26 May 2026

**Copyright:** © 2026 by the authors. Licensee MDPI, Basel, Switzerland. This article is an open access article distributed under the terms and conditions of the Creative Commons Attribution (CC BY) license.

## 1. Introduction

Urban street canyons—narrow corridors enclosed by closely spaced buildings—constitute fundamental morphological units of the built environment [1]. They exert a first-order role influence on wind flow, radiation balance, and pollutant dispersion [2]. Through thermal

storage in building envelopes and ground surfaces, canyon geometries can simultaneously trap heat and attenuate ambient winds, thereby elevating building energy demand for cooling and heating and intensifying urban heat island (UHI) effects [3,4]. The characteristically tight and enclosed morphology of street canyons further promotes pollutant accumulation and impedes natural ventilation [5].

Over the past decades, substantial progress has been made in characterizing steady-state canyon microclimates through full-scale field measurements [6], reduced-scale physical models [7], and computational fluid dynamics (CFD) simulations. These studies have systematically examined the influence of canyon geometry (aspect ratio, orientation, and symmetry), façade properties (albedo), and urban greenery [8] on wind and thermal behavior [9–11]. Pollutant transport within street canyons is governed by two mechanistically distinct air exchange processes: mechanically driven (wind-induced) and thermally driven (buoyancy-induced) exchanges, both of which intensify under conditions of strong ambient wind or elevated canyon surface temperatures [12]. Klein and Galvez [13] demonstrated that wind direction relative to canyon orientation strongly controls the emergence of channeling versus recirculating flows, with implications for turbulence transport and ventilation within the canyon. Zhang et al. [14] investigated diurnal variations in temperature and wind fields in a north–south urban street canyon using thermal balance analysis and large eddy simulation (LES). They found that convective heat transfer from canyon walls dominated the thermal and flow fields, while longwave radiation contributed less than 10% to air temperature changes and had minimal effects ($\leq$2%) on wind velocity and turbulence. This result suggests that the omission of longwave radiation in steady-state CFD models of comparable configurations introduces only minor computational error while substantially reducing computational cost. Growing observational evidence, however, indicates that unsteady atmospheric forcing—including diurnal temperature cycles and transient wind fluctuations—plays an equally important role in shaping canyon microclimates. Field observations consistently reveal pronounced hourly and seasonal variations in both ambient wind velocity and canyon wall temperatures, driven by changes in solar elevation angle, cloud cover fraction, and synoptic-scale weather patterns [15]. Such time-varying disturbances frequently trigger mixed convection regimes in which buoyancy-driven and shear-driven flows interact dynamically. Nevertheless, the transition mechanisms governing these interactions remain insufficiently understood, particularly in full-scale canyons subject to large seasonal contrasts. Many existing CFD studies adopt a steady-state flow assumption or impose overly simplified thermal boundary conditions, which may obscure critical coupling interactions among solar radiation, surface heating, and air flow structure. To better replicate real daytime heating cycles, time-varying heat boundary conditions have been increasingly adopted in recent CFD investigations. Sinusoidal wall temperature inputs work well to catch sun-caused temperature shifts [16]. High-fidelity simulation of urban wind fields, however, entails substantial computational cost, which typically limits studies to short time windows or spatially restricted domains. To address this challenge, Xiang et al. [17] introduced non-intrusive reduced order models (NIROMs) that integrate convolutional autoencoders and XGBoost regression to efficiently predict 3D urban wind fields over extended durations and large domains. These approaches have proven effective in capturing essential airflow characteristics and can support large-scale urban ventilation assessments. Despite these advances, canyon asymmetry remains underrepresented in numerical validations, notwithstanding its strong influence on flow separation, vortex skewness, and wall temperature lags. Moreover, multi-seasonal validation datasets with sufficient temporal resolution are scarce, limiting the predictive transferability of models intended to guide urban design practice [18].

Against this backdrop, it is necessary to explicitly delineate the contributions of the present study relative to the most closely related prior works. Zhang et al. [19] investigated the diurnal evolution of temperature and wind fields in a north–south symmetric canyon using thermal balance analysis and LES, demonstrating that convective wall heat transfer dominates the thermal-flow coupling while longwave radiation exerts negligible influence on wind velocity ($\leq$2%). This work, however, is confined to a single canyon orientation, a single symmetric geometry, and a single diurnal cycle, with thermal boundary conditions derived from a computed energy balance rather than continuous field observations. Consequently, meteorological disturbances such as cold-wave intrusions, intermittent rainfall, and seasonal transitions fall entirely outside its scope. Mei et al. [16] modeled airflow and particle dispersion under a sinusoidal wall temperature boundary condition, showing that idealized sinusoidal inputs can approximate solar-driven heating cycles. Their thermal inputs, however, are prescribed mathematical functions with no observational grounding, and their analysis is restricted to a symmetric canyon under steady ambient wind without considering geometric asymmetry or multi-seasonal variability.

The present study advances beyond these works in four substantive respects. First, all thermal and wind boundary conditions are derived directly from continuous in situ measurements spanning four seasons and 120 monitoring days, encompassing over 360,000 environmental records. This observational foundation allows the numerical simulations to reproduce real meteorological variability, including cold wave cooling and seasonal transitions, that computed or idealized boundary conditions inherently cannot represent. Second, surface temperature characterization is substantially refined: through Levenberg–Marquardt nonlinear curve fitting, this study demonstrates that actual canyon wall temperatures require a piecewise modeling framework rather than a uniform sinusoidal function. Sine functions apply only during consecutive clear sky periods (Stage a, Section 3.2.2), while polynomial functions of varying orders are necessary for cold-wave events (Stage b, Section 3.2.2) and other meteorologically complex episodes (Stages c to e, Section 3.2.2); crucially, the optimal polynomial orders and fitting coefficients differ systematically between symmetric and asymmetric canyons, providing an empirically grounded template for CFD boundary condition specification. Third, this study simultaneously investigates both a symmetric canyon (H/W = 0.82) and an asymmetric canyon (H/W = 2.13 and 0.82) oriented east–west across all four seasons, a paired cross-seasonal design that reveals geometry-dependent phenomena invisible to single-configuration studies, most notably the substantially stronger summer north–south thermal contrast in the asymmetric canyon (10.2 °C versus 3.8 °C) and its qualitatively distinct winter vortex nesting structure in which secondary and tertiary vortices develop and progressively detach within the primary vortex [20]. Fourth, two characteristic ambient wind variation modes, stepwise and gradual, are identified from statistical analysis of the measured time series and linked to distinct mixed convection regimes within the canyon across seasons, a mechanistic connection that has not been previously established with full-scale observational support.

To address these gaps, this study proposes a coupled measurement–simulation framework to characterize the spatiotemporal dynamics of canyon microclimate. Field campaigns were conducted in both symmetric and asymmetric east–west canyons on the Weishui Campus of Chang'an University (Xi'an, China), spanning all four seasons and yielding over 360,000 environmental records. Full-scale CFD models validated against field-measured wind velocities and subjected to systematic grid independence testing were subsequently employed to examine how unsteady wind and thermal forcing govern flow field evolution, vortex dynamics, and vertical heat transfer within the canyon. Compared with existing cross-regional studies conducted in hot-arid climates [9] or temperate oceanic climates [4], this study focuses on the cold climate zone of China, which is prevalent across densely ur-

banized regions of East and Central Asia and characterized by stark seasonal contrasts that drive distinctly different aerodynamic regimes. By combining four seasonal measurements with paired canyon geometries, this study addresses a critical gap in the understanding of long-term microclimate dynamics under extreme seasonal variability.

## 2. Research Methods

### *2.1. Field Measurement*

#### 2.1.1. Target Area

To ensure representativeness of the monitoring results, study sites were selected from canyons whose geometry, surface properties, and surrounding environment reflect typical urban morphologies. Buildings flanking the selected canyons must exhibit adequate length and structural continuity to minimize end effects and building-gap interference on the internal flow field.

Based on the above considerations, a representative symmetric canyon and an asymmetric canyon were selected for detailed field measurement analysis. These canyons are located within the student apartment complex of Chang'an University in Weiyang District, Xi'an City, China. The symmetric canyon is formed between student apartment buildings No. 5 (south side) and No. 6 (north side), both aligned east–west, each comprising five stories with a uniform height of 18 m. In contrast, the asymmetric canyon is formed between Buildings No. 16 and No. 22, also aligned east–west. Building No. 16, located on the north side, is 13 stories high (46.8 m), whereas Building No. 22 on the south side remains five stories tall (18 m). The distance between the two canyon buildings is about 22 m, and the length is about 32 m. Specifically, the symmetric canyon has H/W = 0.82. The asymmetric canyon presents H/W = 2.13 (No. 16) and H/W = 0.82 (No. 22). The location and spatial arrangement of the selected street canyons and their adjacent structures are illustrated in Figure 1.

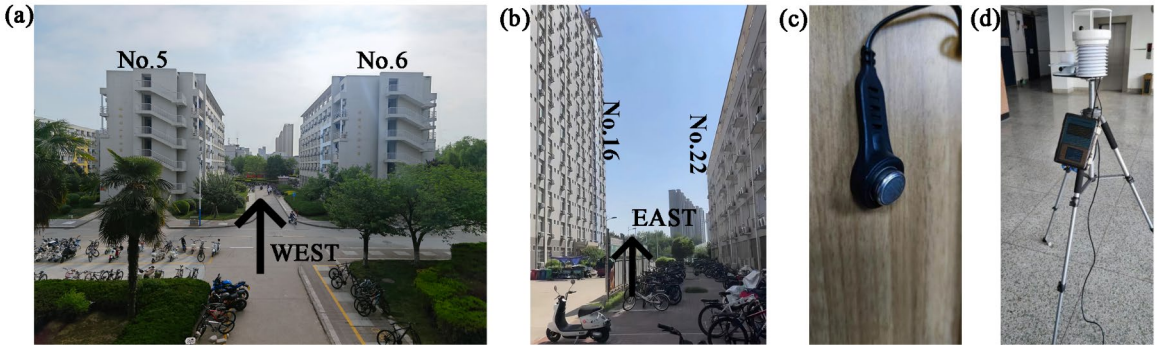


**Figure 1.** Measured canyons and instruments: (**a**) symmetric canyon; (**b**) asymmetric canyon; (**c**) button thermometer; (**d**) portable weather station. ("No. xx" represents the buildings' number and the arrows show the direction of the street axis).

#### 2.1.2. Data Collection

Continuous measurements were conducted in this study using two portable meteorological stations. We recorded key environmental parameters every minute. This frequent timing captured high-resolution variations in the data. These parameters included wind velocity, wind direction, air temperature, and particulate matter concentration. In addition, 12 button thermometers (Figure 1) were deployed to monitor surface temperatures at 10 min intervals. The technical specifications of all monitoring instruments are summarized in Table 1. Yigu Portable Meteorological Station is adopted as the combination of all the listed sensors with the mode code of YGY-CJY-4.

**Table 1.** Detailed specification of the installed instruments.

| Instrument | Model | Resolution | Measuring Range | Accuracy |
|---|---|---|---|---|
| PM2.5/10 particulate matter monitoring sensor | YGY-CJY-4 | 1 μg/m$^3$ | 0–500 μg/m$^3$ | ≤100 μg/m$^3$: ±10 μg/m$^3$; >100 μg/m$^3$: ±10% readings; |
| Ultrasonic wind velocity sensor | YGY-CJY-4 | 0.01 m/s | 0–60 m/s | Start velocity ≤ 0.8 m/s, ±(0.5 + 0.02 v) m/s; |
| Ultrasonic wind direction sensor | YGY-CJY-4 | 1° | 0–359° | ±3% |
| Total solar radiation sensor | TBQ | 1 w/m$^2$ | 0–2000 w/m$^2$ | ±3% |
| Button thermometer | DS1922L | 0.1 °C | −40–85 °C | ±0.1 °C |

The symmetric canyon (Apartments No. 5 and No. 6) was monitored across all four seasons over a total of 78 days, yielding more than 200,000 records. The asymmetric canyon (Apartments No. 16 and No. 22) was monitored during two thermally contrasting seasons—summer and winter—over 42 days, generating more than 160,000 records.

The weather stations were installed on the rooftops. The detailed layout of all measurement points is illustrated in Figure 2. Based on the measured data from the JINGHE-57131099999 station [21], between 1 December 2021 and 26 August 2024, we analyzed the hourly wind direction (Figure 3). The results show a dominant seasonal pattern with NE winds in spring and autumn. In summer, warm and humid air flows from the Pacific Ocean are transported northward along the Wei River Plain, with SE winds dominating. In winter, NE and NW winds alternate, with NE winds gradually dominating in the later stages. The observed correlation between hourly $PM_{2.5}$ and wind velocity is presented in Appendix A (Figures A1 and A2). Seasonal variation in $PM_{2.5}$ concentration under different wind velocity regimes. It shows higher concentration and variability under low wind velocity in winter and autumn, consistent with thermal inversion and recirculating flow regimes. Furthermore, the implications of these distinct vortex structures on pollutant dispersion, specifically PM2.5 concentration distributions, were extensively analyzed as a corollary to the aerodynamic findings. Interested readers are directed to the Appendix A for a detailed discussion on how the aforementioned thermal and flow characteristics directly govern local PM2.5 accumulation and clearance.

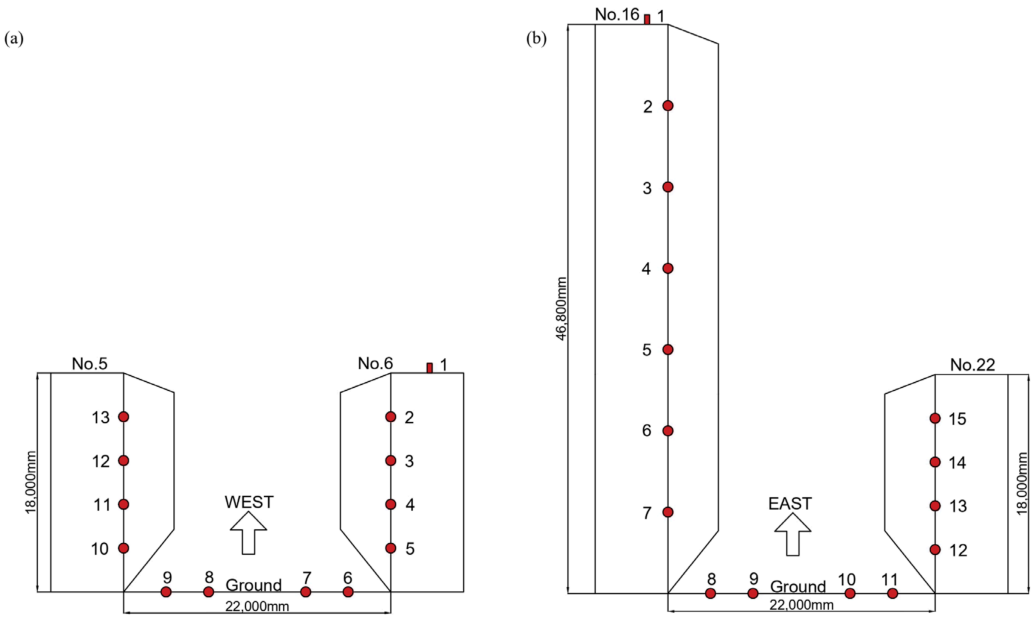


**Figure 2.** Measurement points for the surface temperature: (**a**) symmetric canyon; (**b**) asymmetric canyon.

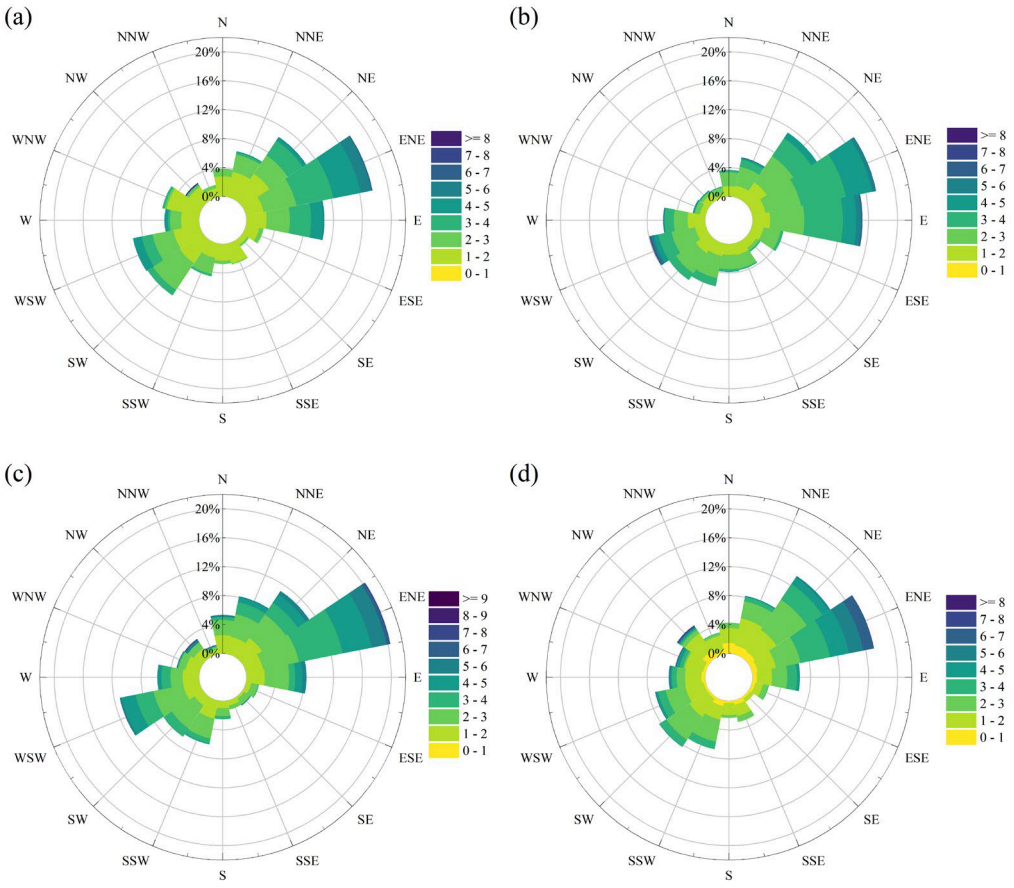


**Figure 3.** Seasonal wind rose diagrams at the JINGHE Station during the observation period, showing dominant wind directions in: (**a**) spring; (**b**) summer; (**c**) autumn; (**d**) winter.

The monitoring campaign for the asymmetric canyon was intentionally concentrated on summer and winter, two thermally extreme seasons, to capture the full range of buoyancy-dominated and wind-dominated flow regimes driven by canyon geometry. Summer and winter bracket the seasonal behavioral spectrum documented and established by the four-season symmetric canyon dataset; spring and autumn represent transitional regimes whose characteristics can be reasonably inferred by interpolation between these two extremes. This targeted approach maximizes the scientific return per monitoring day within constraints of the available project resources.

## *2.2. Numerical Simulation*

### 2.2.1. CFD Model

The numerical model in this study was developed based on a full-scale representation of the actual street canyons. For the symmetric canyon, formed by Apartments No. 5 and No. 6 aligned in the east–west direction, both buildings are 18 m in height, 22 m in width, and 32 m in length. For the asymmetric canyon, consisting of Apartments No. 16 and No. 22, the south-side building (No. 22) is 18 m high, while the north-side building (No. 16) reaches 46.8 m. The canyon width and length are also 22 m and 32 m, respectively.

The simulations were conducted using the Unsteady RANS framework with a time step of 1 s. The simulations were performed using ANSYS Fluent 2023 R1. Pressure–velocity coupling was handled via the SIMPLE algorithm. Spatial discretization employed Second Order Upwind schemes for momentum, turbulent kinetic energy, and turbulent dissipation rate; Second Order Implicit was used for temporal discretization. Convergence was considered achieved when all residuals dropped below $10^{-4}$ at each time

step. Inlet turbulence intensity was set to 5% with a hydraulic diameter of 22 m corresponding to the canyon width. The RNG k-ε turbulence model was selected on the basis of its well-established theoretical suitability for flows with significant streamline curvature and adverse pressure gradients, which are inherent characteristics of separated recirculating flows in deep street canyons. The RNG k-ε model has been extensively validated for urban street canyon simulations in previous studies [5,12]. Near-wall regions were treated using an enhanced wall function approach, with dimensionless wall distance values y+ maintained within the recommended range of 30–200, ensuring adequate resolution of the velocity gradients governing secondary flow separation. The governing equations for the adopted model were as follows:

Continuity equation:

$$\frac{\partial \rho}{\partial t} + \frac{\partial (\rho u_i)}{\partial x_i} = 0 \tag{1}$$

Momentum equation:

$$\frac{\partial (\rho u_i)}{\partial t} + \frac{\partial (\rho u_i u_j)}{\partial x_j} = -\frac{\partial p}{\partial x_i} + \frac{\partial}{\partial x_j}[\mu_{eff}(\frac{\partial u_i}{\partial x_j} + \frac{\partial u_j}{\partial x_i})] + \rho g_i \beta (T - T_{ref}) \tag{2}$$

Energy equation:

$$\frac{\partial (\rho c_p T)}{\partial t} + \frac{\partial (\rho c_p u_j T)}{\partial x_j} = \frac{\partial}{\partial x_j}[(\lambda + \frac{c_p \mu_t}{\mathrm{Pr}_t})\frac{\partial T}{\partial x_j}] \tag{3}$$

Turbulent kinetic energy equation:

$$\frac{\partial (\rho k)}{\partial t} + \frac{\partial (\rho k u_i)}{\partial x_i} = \frac{\partial}{\partial x_j}[\alpha_k \mu_{eff} \frac{\partial k}{\partial x_j}] + G_k + G_b - \rho \varepsilon \tag{4}$$

Energy dissipation equation:

$$\frac{\partial (\rho \varepsilon)}{\partial t} + \frac{\partial (\rho \varepsilon u_i)}{\partial x_i} = \frac{\partial}{\partial x_j}[\alpha_\varepsilon \mu_{eff} \frac{\partial \varepsilon}{\partial x_j}] + C_{1\varepsilon} \frac{\varepsilon}{k}(G_k + C_{3\varepsilon} G_b) - C_{2\varepsilon} \rho \frac{\varepsilon^2}{k} - R_\varepsilon \tag{5}$$

where $\mu_{eff}$ is the effective dynamic viscosity, which is the summation of molecular viscosity and turbulent viscosity; $\beta$ is the thermal expansion coefficient of air; $T$ is the local air temperature; $T_{ref}$ is the reference ambient temperature; $\lambda$ represents the coefficient of thermal conductivity; $\alpha_k$ is the inverse effective Prandtl number for $k$ diffusion; $C_{1\varepsilon}$, $C_{2\varepsilon}$, and $C_{3\varepsilon}$ are constant in the turbulence model (the values are 1.42, 1.68 and 1.0, respectively); $G_b$ denotes the turbulent kinetic energy generated by buoyancy forces; and $R_\varepsilon$ is the additional rate-of-strain term unique to the RNG formulation.

$$R_\varepsilon = \frac{C_\mu \rho \eta^3 (1 - \frac{\eta}{\eta_0})}{1 + \beta_0 \eta^3} \cdot \frac{\varepsilon^2}{k} \tag{6}$$

Following the relevant suggestions of the AIJ (Architectural Institute of Japan) Guidelines [20], the maximum building height ($H$) within each canyon was used as the characteristic length scale. The top surfaces of the buildings were treated as slip walls, the upper boundary of the computational domain. The inlet boundary was placed 5$H$ upstream from the leading edge of the canyon, and the outlet boundary was located 15$H$ downstream. The canyon length ($L$) in the model corresponds to the actual physical length, as presented in Figure 4.

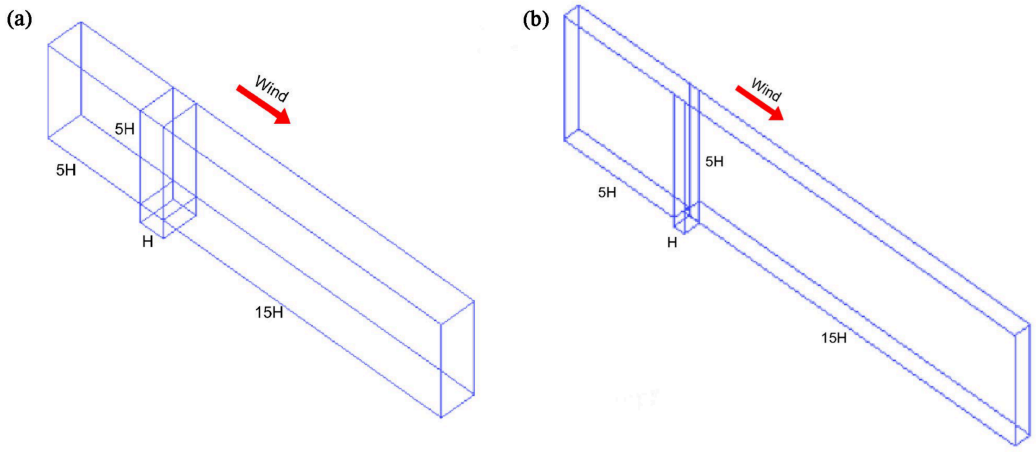


**Figure 4.** Computational domain: (**a**) symmetric canyon; (**b**) asymmetric canyon.

The boundary conditions for wind and thermal disturbances were determined based on field measurements obtained in Xi'an, Shaanxi Province. A no-slip boundary condition was applied to all canyon surfaces. The inlet was defined as a velocity inlet, where the airflow properties were specified. The outlet boundary was set as a fully developed outflow, based on the sufficiently long domain ensuring flow development. A gauge pressure of zero was applied at the outlet to complete the boundary setup.

Solar effects and wall heating are represented exclusively through measured and fitted wall-surface temperatures imposed as time-varying thermal boundary conditions via User-Defined Functions. It is explicitly acknowledged that humidity transfer, explicit radiative exchange, wall heat storage, and full surface energy balance modeling are not independently solved within this framework. These processes are handled implicitly: the measured wall temperatures encapsulate the net result of solar absorption, heat storage, and longwave radiation under the specific site conditions. This simplification is acknowledged as a limitation of the present study.

#### 2.2.2. Model Validation

To assess the sensitivity of simulation results to spatial discretization, six grid schemes were tested for the symmetric canyon model, using wind velocity at selected monitoring points as the evaluation metric. As shown in Figure 5a and Table 2, wind velocity predictions became insensitive to further mesh refinement once the total cell count exceeded 1,455,681, confirming that grid independence was achieved at this resolution. The mesh comprising 1,455,681 cells was therefore adopted for all subsequent simulations. Therefore, the grid with 1,455,681 cells was adopted for all subsequent simulations of the canyon wind and thermal environment. Grid independence verification was explicitly conducted for the symmetric canyon, as described above. For the asymmetric canyon, the same meshing methodology, near-wall refinement settings, and turbulence model configuration were applied, with the total cell count increased proportionally to accommodate the greater wall surface area of the taller windward building. The good agreement between simulated and measured flow field structures and thermal distributions in the asymmetric canyon across both monitored seasons provides indirect validation of the mesh adequacy. Explicit grid independence testing for the asymmetric canyon is identified as a priority for future work.

For model validation, simulated wind velocities were compared with field measurements. Using measured meteorological variables and wall-surface temperatures at 10 min intervals for a winter day as boundary conditions, wind velocity along the X-axis at Point A (1.5 m above ground along the canyon centerline) was simulated and evaluated against observations. As shown in Figure 5b, the maximum error was 7.26%, indicating good

agreement and confirming the model's capability to reproduce the canyon wind field with acceptable accuracy.

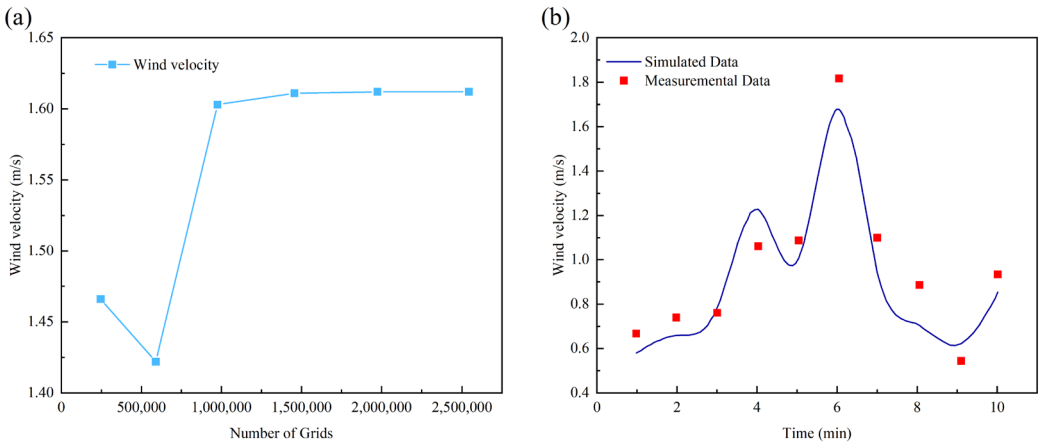


**Figure 5.** Model validation: (**a**) grid independence; (**b**) model accuracy validation.

**Table 2.** Grid independence verification.

| Number of Grids | Height of the First–Layer Grid (m) | Maximum Grid Scale (m) | Number of Nodes per 10 m | Point A Velocity (m/s) |
|---|---|---|---|---|
| 245,812 | 0.2 | 0.9 | 5 | 1.466 |
| 589,845 | 0.15 | 0.8 | 8 | 1.422 |
| 975,427 | 0.1 | 0.8 | 10 | 1.603 |
| 1,455,681 | 0.09 | 0.6 | 15 | 1.611 |
| 1,974,287 | 0.08 | 0.5 | 18 | 1.612 |
| 2,543,266 | 0.05 | 0.4 | 25 | 1.612 |

To further assess the model's reliability, the validation was extended to include both winter and summer field measurements, with surface temperature incorporated as an additional evaluation parameter alongside wind velocity. The validation dataset was drawn from two distinct seasonal monitoring campaigns covering meteorologically contrasting conditions: the Winter case dataset spans 2–3 December 2022 (2 days, 48 data pairs at 60 min intervals), representing cold season regimes, while the Summer case dataset spans 20–21 July 2023 (2 days, 48 data pairs at 60 min intervals), representing warm season regimes. Simulated wind velocities and surface temperatures were compared with field observations for both seasons. The agreement between simulated and measured values was quantified using three statistical indices: Root Mean Square Error (RMSE), Mean Absolute Error (MAE), and the coefficient of determination ($R^2$), defined as:

$$\mathrm{RMSE} = \sqrt{\frac{1}{n}\sum_{i=1}^{n}(S_i - O_i)^2} \tag{7}$$

$$\mathrm{MAE} = \frac{1}{n}\sum_{i=1}^{n}|S_i - O_i|^2 \tag{8}$$

$$\mathrm{R}^2 = 1 - \frac{\frac{1}{n}\sum_{i=1}^{n}(S_i - O_i)^2}{\frac{1}{n}\sum_{i=1}^{n}(O_i - \overline{O})^2} \tag{9}$$

where $S_i$ represents the simulated value of a flow variable at time interval $i$, and $O_i$ represents the corresponding measured value recorded by the on-site instruments at the same location and the same time. Each value of $i$ corresponds to one 60 min averaged

observation record, consistent with the logging interval of the field instruments deployed in this study. $\overline{O}$ is the mean of observed values, and $n$ is the total number of comparison points. The calculated statistical indices are summarized in Table 3.

**Table 3.** Model validation statistics.

| Parameter | Season | RMSE | MAE | $R^2$ |
|---|---|---|---|---|
| Wind velocity (m/s) | Winter | 0.18 | 0.14 | 0.92 |
| Wind velocity (m/s) | Summer | 0.21 | 0.16 | 0.90 |
| Surface temperature (°C) | Winter | 0.85 | 0.67 | 0.94 |
| Surface temperature (°C) | Summer | 1.12 | 0.89 | 0.91 |

Wind velocity predictions yielded $R^2$ = 0.92 and $R^2$ = 0.90 for winter and summer, respectively, consistent with the single-day maximum error of 7.26% reported above. Surface temperature predictions achieved $R^2$ = 0.94 (winter) and $R^2$ = 0.91 (summer), confirming that the model reliably reproduces both wind and thermal characteristics across seasons. It should be noted that turbulence intensity was not included as a validation parameter due to instrument limitations, and this is identified as a limitation of the current study.

## 3. Results and Discussion

### *3.1. Measured Ambient Wind*

Characterizing the dynamic properties of ambient winds is essential for informing evidence-based canyon design strategies, mitigating UHI effects, and predicting air quality within street canyons. Urban airflow is inherently turbulent, exhibiting stochastic temporal fluctuations that necessitate statistical analysis for meaningful interpretation.

In this research, the average value of the observed sample data at spatial points over a time period can be taken, and the average wind velocity can be used to study its pulsation characteristics, and its calculation formula is as follows:

$$\overline{v}_i = \frac{1}{t_2 - t_1} \int_{t_1}^{t_2} v_i(t) dt \tag{10}$$

$$v_t = \overline{v} + v'_t \tag{11}$$

where $t_1$ and $t_2$ represent the initial and final moments of a certain moment, $\overline{v}_i$ is the average wind velocity at time $t_1$ to $t_2$, $v_i(t)$ is the instantaneous wind velocity at time $t$.

According to the statistical analysis presented in Figure A3 and Table 4, both instantaneous and average wind velocities exhibit clear seasonal variations. In general, the asymmetric street canyon demonstrates higher peak values of instantaneous and average wind velocities compared to the symmetric canyon across the same seasons. This phenomenon can be attributed to the height difference between buildings in the asymmetric canyon (Figure A4), where the taller structures on one side create a channeling and acceleration effect for incoming airflow. Ground temperature increases rapidly in the morning and reaches its peak before noon, consistent with the ground remaining within the directly irradiated zone during this period. The south-facing wall exhibits a gradual temperature rise in the afternoon, reflecting its progressive exposure to direct solar radiation as the sun's azimuth shifts. In contrast, the north-facing wall remains largely shaded throughout the day, exhibiting minimal diurnal temperature variation. This stability is typical of a shaded facade. These spatially differentiated thermal responses validate the intentional placement of measurement points, confirming that the monitoring network successfully captured the transitions between directly irradiated and shaded surface zones.

**Table 4.** Seasonal maximum wind velocities in symmetric and asymmetric street canyons.

| Season | Symmetric Canyon (m/s) | Asymmetric Canyon (m/s) |
|---|---|---|
| | Instantaneous/Average | Instantaneous/Average |
| Spring | 3.14/2.78 | -/- |
| Summer | 4.44/3.82 | 4.91/4.11 |
| Autumn | 4.28/4.28 | -/- |
| Winter | 6.77/5.84 | 11.14/6.85 |

These distinct thermal responses confirm our intentional placement of measurement points. We successfully captured the transitions between sunlit and shaded areas.

Statistical analysis of the instantaneous and time-averaged wind velocity records reveals two distinct variation modes in the ambient wind measured above the canyon (Figure A5), hereinafter classified as the stepwise mode and the gradual mode.

### *3.2. Measured Surface Temperature*

#### 3.2.1. Seasonal Temperature Variation of Street Canyon Surfaces

The seasonal air temperature statistics for the symmetric street canyon (winter, spring, summer, and autumn) and the asymmetric street canyon (summer and winter) are presented in Figure 6. These figures illustrate the temporal variation in air temperature across different seasons. In the visual representation, red shading indicates periods of clear and sunny weather, while blue shading denotes episodes of rainfall or temperature decline. Additionally, the transparency of the color shading is employed to reflect the relative magnitude of air temperature: higher transparency corresponds to higher temperature values, whereas lower transparency indicates cooler conditions.

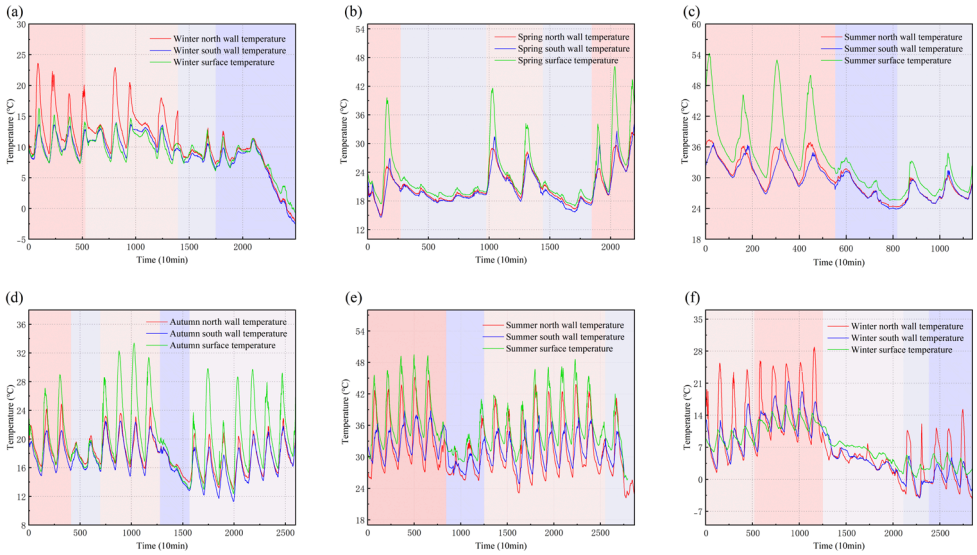


**Figure 6.** Wall temperature variation in symmetric street canyon: (**a**) in winter; (**b**) in spring; (**c**) in summer; (**d**) in autumn; in asymmetric street canyon: (**e**) in summer; (**f**) in winter. (The red background indicates sunny days, and the blue background indicates cloudy and rainy days. The transparency of the colors represents the relative air temperature, with higher transparency indicating higher temperatures).

In the symmetric street canyon, wall and ground temperatures exhibit pronounced seasonal variability. Winter is the only season in which the north-facing wall attains the highest temperature among all monitored surfaces. During winter, the south-facing wall and ground surface reach comparable temperatures, though the south wall's diurnal peaks

slightly exceed that of the ground. In spring, summer, and autumn, the ground surface consistently registers the highest temperatures, while the north–south wall temperature differential remains relatively small. In spring, the south wall is generally warmer than the north wall; however, during cold-wave events, the south wall undergoes more intense cooling, causing its peak temperatures to fall below that of the north wall. In summer and autumn, ground surface temperatures remain dominant, and the north wall is only marginally warmer than the south wall. Regarding diurnal timing, peak temperatures on the ground and north wall consistently precede those on the south wall in spring and summer, indicating a delayed thermal response of the south wall; this thermal lag diminishes in autumn and becomes negligible in winter.

The asymmetric canyon shows broadly similar seasonal behavior. In summer, the ground is the warmest surface, and the north wall reaches higher peak temperatures than the south wall; in winter, the north wall remains the warmest surface. Compared with the symmetric canyon, the asymmetric canyon exhibits a stronger summer thermal contrast between north and south walls, with a maximum difference of 10.2 °C versus 3.8 °C. In winter, the ground surface is the coldest in the asymmetric canyon, whereas in the symmetric canyon, it is slightly warmer than the south wall. During winter cold-wave events, both canyons show the smallest temperature reduction at the ground, which often becomes the warmest surface. The north wall peaks earlier than the south wall in summer, and this timing offset also persists in winter in the asymmetric canyon, suggesting a more stable and intensified directional heating effect.

#### 3.2.2. Cross-Seasonal Temperature Variation of Street Canyon Surfaces

Surface temperature in street canyons plays a key role in shaping the local wind and thermal environment. To characterize cross-seasonal wall-surface temperature evolution, long-term measurements were analyzed using nonlinear curve fitting. A piecewise modeling strategy was adopted, in which the long-term temperature time series for each season was segmented according to prevailing meteorological conditions, and each segment was fitted with the most physically appropriate mathematical function. Taking the north-facing wall temperature in winter within the symmetric street canyon as an illustrative example (Figure 7), consecutive sunny days produced approximately periodic diurnal oscillations (Stage a) that were best described by a sine function. The subsequent cold-wave-induced cooling following the sunny period (Stage b) was better represented by polynomial functions. Additional episodes involving brief warming followed by cooling (Stages c–e) were likewise fitted using polynomials. This piecewise combination of trigonometric and polynomial functions enables improved representation of nonlinear surface temperature behavior and abrupt meteorological transitions, thereby supporting both mechanistic interpretation and quantitative forecasting. In summary, sine functions were most appropriate for characterizing periodic diurnal variation under clear-sky conditions, whereas polynomial functions of increasing order provide the flexibility necessary to capture irregular and complex temperature fluctuations during meteorologically disturbed periods such as cold-wave events. Model performance was evaluated using the coefficient of determination ($R^2$), and all fitted curves achieved $R^2 > 0.7$, indicating satisfactory fit and the appropriateness of the selected formulations. Due to the large amount of measured data, the fitting of the north wall surface of the symmetric street canyon in winter, as well as the asymmetric street canyon in winter, will be taken as an example; other fitting figures are attached in Appendix A (Figure A6, etc.).

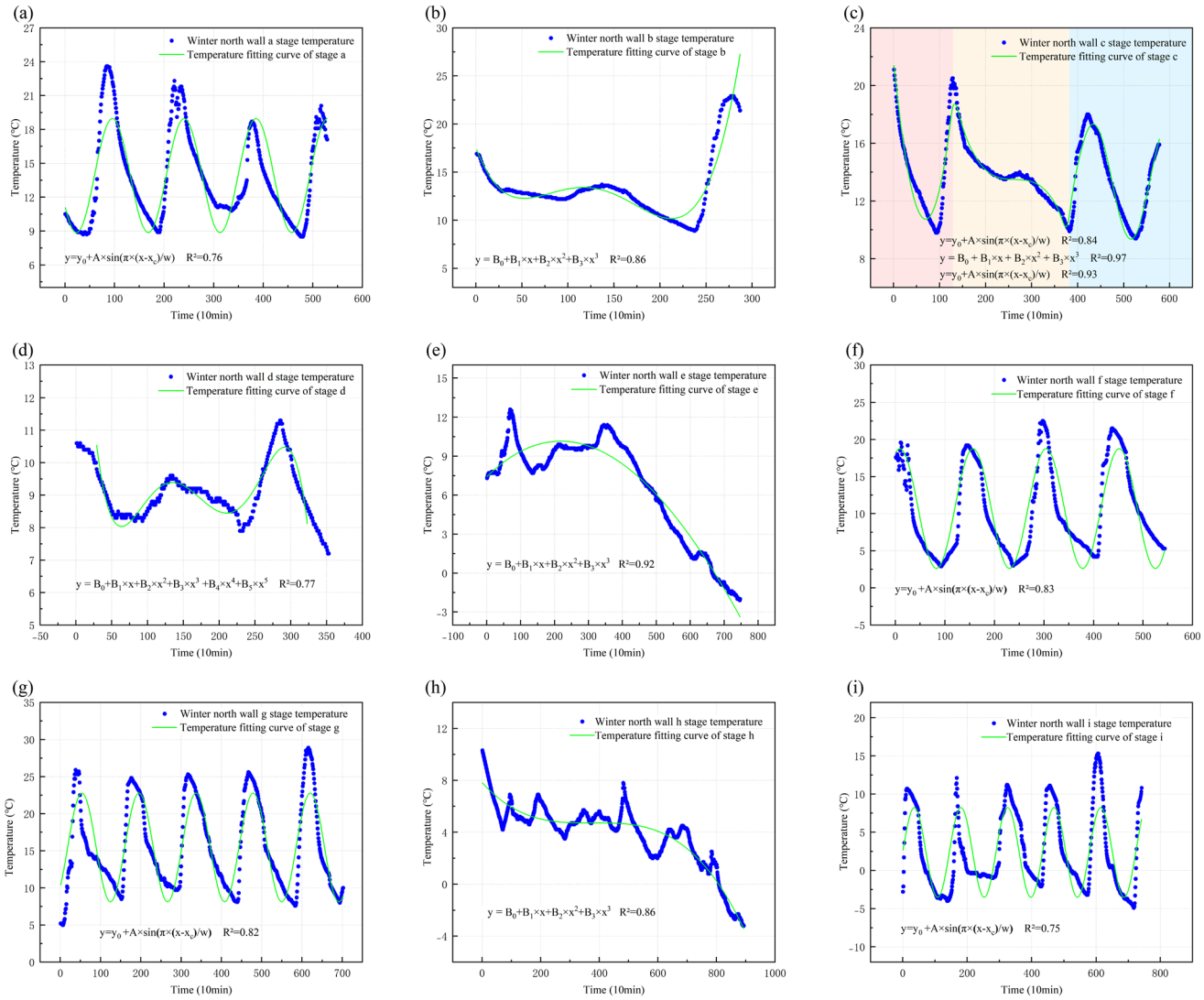


**Figure 7.** Fitting curves for north wall surface temperatures in symmetric (phases (**a**–**e**)) and asymmetric (phases (**f**–**i**)) street canyons during winter (Different background colors indicate the different formulas used for data fitting.).

To further demonstrate the advantage of the piecewise approach, a single sine function uniformly across all stages of the north wall winter temperature series in the symmetric canyon is applied with the same dataset used in Figure 7. For Stage a (consecutive sunny days), both methods achieve comparable $R^2$ values (0.81 vs. 0.83), confirming that sine functions are appropriate under clear-sky conditions. However, for Stage b (cold-wave cooling) and Stages c–e (post-cold-wave rebound and fluctuation), the single sine function yields $R^2$ values of 0.31, 0.28, and 0.35, respectively, failing to capture the monotonic decline and irregular multi-stage recovery. By contrast, the piecewise polynomial functions achieve $R^2 > 0.70$ for all stages, representing a substantial improvement in fit quality. These results confirm that the piecewise framework is not only more accurate but also physically more appropriate: it avoids imposing artificial periodicity on temperature episodes that are fundamentally non-periodic in nature. The surface temperature functions (sine and polynomial) derived from field data were used to define the wall boundary conditions.

In a symmetric street canyon, wall temperature trends show that during winter, the north wall tends to be warmer than the surface, which in turn is warmer than the south wall. However, during cold wave events, the peak surface temperature surpasses that of both the north and south walls. In this study, cold wave events are identified according to the

China Meteorological Administration standard (CMA GB/T 21987-2017) [22]: a cold wave is defined as any event in which the 24 h surface air temperature drop exceeds 8 °C, the 48 h drop exceeds 10 °C, or the 72 h drop exceeds 12 °C, with a concurrent daily minimum temperature at or below 4 °C. All subsequent references to 'cold wave' conditions in this paper refer to monitoring periods satisfying this criterion.

During the 22-day winter monitoring period for the symmetric canyon (14 November to 5 December 2022), one primary cold-wave event was identified. The event lasted four days, from 21 to 25 November 2022. It satisfied the CMA criterion on the basis of a 24 h temperature drop of 11.5 °C recorded between 21 and 22 November, exceeding the required threshold of 8 °C, accompanied by a daily minimum temperature below 4 °C. The conditions of 22 November correspond specifically to Stage b in the piecewise fitting framework, representing the cold-wave cooling phase used to derive the polynomial thermal boundary conditions for the Winter Cold Wave CFD simulation in Section 3.3.

In spring, summer, and autumn, the surface consistently exhibits the highest temperatures, with the north wall showing a more rapid warming and cooling trend compared to the south wall.

In an asymmetric street canyon, summer temperatures follow the trend: surface > north wall > south wall. However, the temperature difference between the surface and the north wall is smaller than that observed in symmetric street canyons. In winter, the trend shifts to: north wall > south wall > surface.

From the fitting function analysis, it is evident that the sine function under sunny conditions can accurately represent the wall temperature variation trends, as shown in Equation (3). In the sine function, the coefficient $A$ represents the amplitude. Fitting results indicate that under clear winter conditions, the amplitude of wall temperature variations in both symmetric and asymmetric canyons is greater than in other seasons. The amplitude follows a seasonal pattern, gradually increasing from summer to winter. Statistical data show that in winter, the maximum surface temperature difference between daytime peak and nighttime low can reach up to 23 °C. In contrast, during summer—when the solar altitude is at its highest and sunlight duration is longest—the maximum wall temperature difference is about 16.7 °C. Other parameters of the sine function, such as $y_0$, $x_c$ and $w$, vary with the seasons and corresponding meteorological conditions.

$$y = y_0 + A \sin \frac{\pi(x - x_c)}{w} \tag{12}$$

The piecewise fitting framework proposed in this study offers three methodological advantages over the conventional single-function approach. First, it explicitly accounts for weather-state diversity: real urban surface temperatures comprise multiple meteorologically distinct episodes within a single season, and a single sinusoidal assumption as employed by Mei et al. (2017) [16] cannot structurally represent cold-wave cooling, rebound warming, or intermittent fluctuation stages. Second, the framework is geometry-sensitive: fitting parameters, including sine amplitude and polynomial order, differ systematically between symmetric and asymmetric canyons. Specifically, the sine amplitude increases from summer to winter in the symmetric canyon, while the asymmetric canyon exhibits a comparatively smaller amplitude difference between seasons, reflecting its more sheltered thermal environment. Polynomial order requirements also vary with both weather type and canyon geometry, revealing a regularity that has direct implications for parameterizing thermal boundary conditions for canyons of varying H/W ratios. Third, the framework is practically transferable: by classifying incoming weather conditions into the identified stages (a–e for the symmetric canyon; f–i for the asymmetric canyon), practitioners can select the appropriate function type and parameter range to pre-specify surface temper-

ature inputs for CFD simulations of canyons with known geometry, without relying on idealized assumptions or computationally expensive thermal balance models. It must be emphasized, however, that the specific fitting coefficients reported here are strictly valid for the monitored canyons under the local continental monsoon climate of Xi'an; applying this methodology to other sites requires new field measurement campaigns to derive site-specific coefficients appropriate to the local climate and canyon geometry.

The fitted diurnal functions derived above are used directly as time-varying thermal boundary conditions on the canyon wall surfaces in the CFD simulations presented in Section 3.3, enabling the wind field and vortex structure analysis to reflect physically representative seasonal surface thermal forcing rather than idealized constant-temperature assumptions.

The shape and phase characteristics of the fitted diurnal surface temperature polynomials are physically consistent with the thermal properties of the reinforced concrete and brick masonry construction of the monitored buildings. The moderate volumetric heat capacity produces a measurable lag between peak solar irradiance and peak sensible heat release, contributing to the delayed afternoon temperature maxima in the monitoring records. The pronounced north–south temperature asymmetry, particularly the 10.2 °C differential in the asymmetric canyon in summer, further reflects the low albedo of the concrete surfaces, which maximizes net radiation absorption on directly irradiated walls and intensifies buoyancy-driven convective circulation within the canyon.

### *3.3. Simulation Results*

#### 3.3.1. Seasonal Differences of Symmetric Canyon

Figure 8 illustrates the streamlines within the street canyon at 12:00 across the four seasons. As previously analyzed, it is evident that seasonal variations significantly influence the flow field and thermal environment within the street canyon at the same moment in time.

In spring, the flow field is shaped by gradually increasing solar radiation and the rebound of ambient air temperature. These changes lead to a transition from weak vortex activity to progressively stronger convective motion. The increase in surface temperature induces updrafts, forming vortex structures near the canyon center. These vortices promote vertical heat transfer and enhance localized air circulation.

During summer, the solar elevation angle reaches its annual maximum, and by 8:00, the sun's position already corresponds to that observed at approximately 10:00 in spring and autumn. This earlier onset of intense irradiance advances the timing of vortex formation and development. The combination of peak solar radiation and elevated ambient temperatures produces highly dynamic flow field behavior: intensified thermal convection amplifies vortex activity, yielding larger and more energetic vortex structures, enhanced heat accumulation at vortex cores, and more pronounced thermal gradients along the canyon walls.

In autumn, declining ambient temperatures and reduced solar radiation collectively promote a more stable flow field. Compared with spring and summer, streamline patterns and vortex morphologies become more regular and spatially uniform. Solar radiation continues to govern the surface temperature distribution, but its reduced intensity weakens vortex activity; the central vortex exhibits an outward spreading tendency, indicative of a transition toward more moderate convective behavior. To ensure representativeness of the monitoring results, study sites were selected from canyons whose geometry, surface properties, and surrounding environment reflect typical urban morphologies. Buildings flanking the selected canyons must exhibit adequate length and structural continuity to minimize end effects and building-gap interference on the internal flow field [16].

In general, the seasonal changes in canyon airflow patterns show how solar radiation affects wall temperatures, which then have an impact on the intricate aerothermodynamic and heat transfer mechanisms inside the canyon, and these differences manifest through distinct vortex morphologies, orientations, and formation times across seasons.

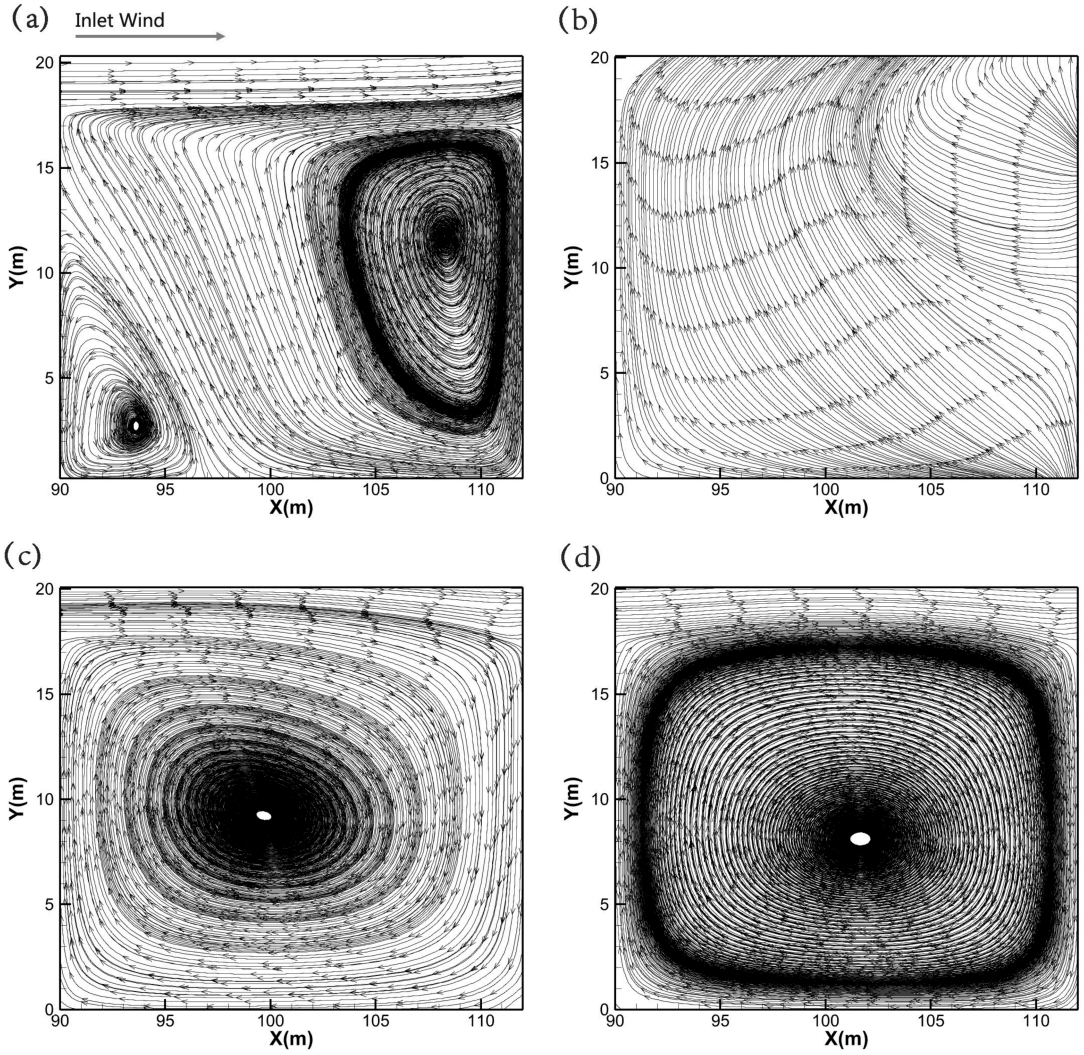


**Figure 8.** Instantaneous streamlines and air temperature contours at 12:00 across four seasons in the symmetric street canyon: (**a**) winter cold-wave; (**b**) spring; (**c**) summer; (**d**) autumn. Inlet wind blows from South (Windward) to North (Leeward), perpendicular to the East–West canyon axis.

### 3.3.2. Seasonal Differences of Asymmetric Canyon

The seasonal disparities in airflow configurations and thermal settings within an asymmetric street canyon between the bright summer and overcast winter emphasize how significantly natural elements impact the wind patterns and microclimate there, and Figure 9 presents typical flow fields at 10:00, 12:00, and 14:00 during both summer and winter.

On a clear summer day, intense solar irradiance rapidly heats both the ground surface and the canyon walls, substantially intensifying thermal convection. A dominant vortex develops on the leeward side of the canyon, accompanied by a smaller secondary vortex at the base of the windward wall. The dynamic evolution of these vortex structures promotes effective vertical heat transfer and enhances local air mixing within the canyon.

During the day, alterations in the flow field mainly revolve around the large principal vortex located on the left side of the canyon and the boundary of this principal vortex

slowly shrinks and grows more diffusive as time passes while at the same time the small vortex close to the windward wall shows an increasing intensification tendency during that period which adds to the overall summer airflow behavior dynamics.

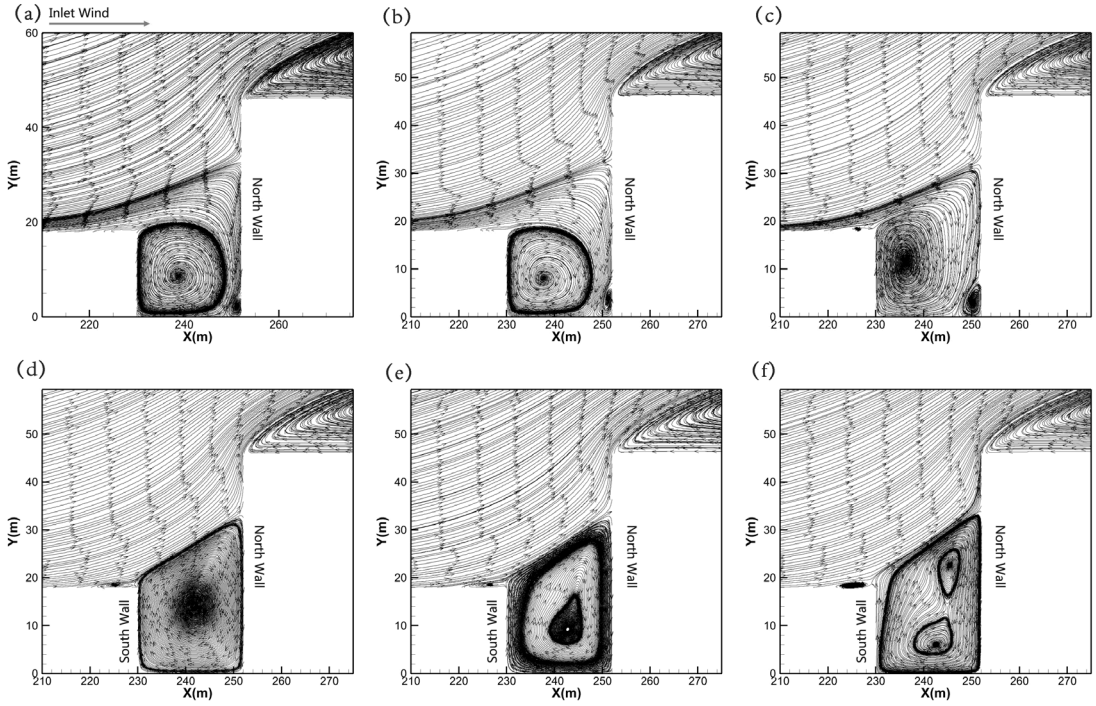


**Figure 9.** Instantaneous streamlines and air temperature contours at 10:00, 12:00, and 14:00 in the asymmetric street canyon under summer (**a**–**c**) and winter cold-wave (**d**–**f**) conditions.

In the contrary, during the winter cold waves events, the absece of significant solar radiation greatly dimishes wall surface, resulting in weak thermal convection. Under these conditions, the canyon airflow is predominantly governed by the elevated ambient wind velocity associated with cold-wave intrusion, which severely disrupts the internal flow structure and generates multiple vortices distributed throughout the canyon cross-section—a pattern markedly different from the summer configuration.

Unlike the spatially constrained vortex observed in summer, winter vortices expand to occupy the full canyon cross-section, producing a more complex and turbulent flow pattern. A secondary vortex develops within the primary vortex, and as time progresses, a tertiary vortex emerges within the secondary structure. This tertiary vortex then gradually detaches from its parent structure, indicating the evolution of a highly stratified and dynamically unstable flow field under winter forcing conditions.

In summary, under strong solar heating on a clear summer day, the primary canyon vortex shifts toward the downwind wall, and a small vortex at the foot of the windward wall intensifies during daytime to enhance in canyon heat exchange; by contrast, under winter conditions without solar radiation, a strong cold wind dominates the flow, leading to the formation of multiple vortices inside the canyon, including the development and shedding of secondary and tertiary vortices [6]. These seasonal differences reflect a shift from an unstable buoyancy-driven flow regime in summer to a strong wind-driven turbulent regime in winter, which significantly alters the canyon's ventilation performance and thermal comfort.

While this study provides comprehensive insights into the wind-thermal microclimate of street canyons, several limitations must be acknowledged to contextualize the findings and guide future research. First, regarding instrument accuracy, the ultrasonic wind sensors deployed in the field campaigns possess a starting velocity threshold ($\leq$0.8 m/s), which

restricted the precise capture of high-frequency turbulent fluctuations and the calculation of turbulence intensity under low-wind conditions. Future campaigns should incorporate high-frequency 3D sonic anemometers to resolve fine-scale turbulence. Second, concerning simulation assumptions, the CFD model was based on the unsteady state RANS approach and idealized physical geometries. Although highly reliable for time-averaged macroscopic fields, it inherently filters out transient turbulent structures and omits the micro-scale effects of street trees, traffic-induced turbulence, and anthropogenic heat emissions. Subsequent studies should aim to utilize transient Large Eddy Simulation (LES) coupled with dynamic vegetation and anthropogenic heat models to capture these complex interactions. Finally, while the measurement duration spanned multiple seasons, the data collection was episodic rather than continuous over long periods. Establishing permanent, multi-year monitoring networks will be essential in future research to assess inter-annual microclimate variability and the specific impacts of extreme weather events, thereby further validating the wind-thermal-pollutant coupling mechanisms identified in this study.

The sensitivity of canyon vortex morphology to the stepped and gradual thermal forcing modes differs substantially between canyon geometries. Under stepped forcing, the asymmetric canyon exhibits pronounced structural sensitivity, including rapid vortex core displacement, intermittent secondary vortex generation, and transient vortex splitting under extreme cold-wave onset conditions, all driven by the geometric amplification of abrupt buoyancy gradient reversals. Under gradual sinusoidal forcing, vortex morphology evolves quasi-statically with high temporal predictability in both canyon types, with the asymmetric canyon maintaining a persistently stratified multi-vortex hierarchy throughout the daytime heating period. The symmetric canyon demonstrates comparatively lower structural sensitivity to both forcing modes, as the symmetric thermal boundary conditions suppress the lateral buoyancy gradients responsible for the more complex vortex dynamics observed in the asymmetric configuration.

## 4. Conclusions

This study offered a full-fledged statistical analysis founded on 120 successive days of on-site measurement data, concentrating on two crucial parameters, namely the ambient wind patterns and the wall surface temperature in both symmetrical and asymmetrical street canyons, and the principal findings were summarized below:

(a) Ambient wind patterns within both symmetric and asymmetric street canyons can be generalized into two typical variation forms based on average wind velocity: stepped variation and gradual variation.

(b) In the symmetric canyon, the dominant seasonal surface temperature hierarchy during winter follows the order: north wall > ground surface > south wall. During cold-wave intrusion events, however, ground surface peak temperatures transiently surpass those of both walls. In all other seasons, the ground surface consistently registers the highest temperatures, with the north wall exhibiting faster diurnal warming and cooling rates relative to the south wall. In the asymmetric canyon, the summer temperature hierarchy follows: ground surface > north wall > south wall, though the differential between the ground surface and north wall is less pronounced than in the symmetric configuration. In winter, the hierarchy reverses to: north wall > south wall > ground surface.

(c) A regression analysis was carried out by means of Origin software, with the north wall temperature taken as an example. Sine functions were utilized for long-term fitting during continuously sunny days, which enabled us to understand the daily temperature variations, and at the same time, polynomial functions were more appropriate for simulating seasonal changes (the warming and cooling stages). The empirical polynomial models for diurnal surface temperature reveal distinct thermal response patterns between

the two studied configurations. To accurately capture the intensified asymmetric solar shading and radiation trapping effects in the asymmetric canyon, the fitting equations exhibited significant variations in polynomial coefficients and required different mathematical structures compared to the symmetric canyon. These specific empirical formulas and fitting coefficients are valid strictly for the monitored canyons under the local continental monsoon climate; their direct numerical application to other sites is not recommended without independent measurement campaigns. The piecewise fitting strategy itself, however, is transferable across climatic zones and canyon geometries, provided that site-specific coefficients are locally calibrated.

(d) Simulations reveal distinct seasonal behaviors: In symmetric canyons, spring temperatures induce complex vortices; summer experiences early vortex formation; autumn flow stabilizes; winter cold waves generate two distinct vortices. Asymmetric gorges present more pronounced distinctions, as in summer, there were dynamic and unstable vortices resulting from thermal differences, whereas winter develops a nested system (primary vortex with secondary and detaching tertiary vortices), creating stratified flow structures.

Beyond their descriptive role, the piecewise surface temperature fitting functions developed in this study constitute a practical predictive framework for urban microclimate modeling. By classifying prevailing weather conditions into the identified meteorological stages and selecting the corresponding function type sine for clear-sky periods, polynomial for cold-wave and transitional episodes, future studies can efficiently prescribe realistic thermal boundary conditions for CFD simulations of street canyons with varying geometries, without relying on idealized sinusoidal assumptions or computationally intensive thermal balance calculations. It is acknowledged that cross-site validation, applying the fitted functions to an independent monitoring dataset from a different campus or city, would further substantiate the generalizability of this framework. This is identified as a priority direction for future work. Furthermore, while the specific temperature fitting coefficients derived in this study reflect the local continental monsoon climate, the proposed methodological framework exhibits broad regional applicability. The piecewise fitting strategy and the measurement-driven CFD boundary condition setup can be seamlessly transferred to other climatic zones. Future cross-regional research should apply this framework to contrasting climates to validate its universal applicability and to establish a comprehensive, climate-specific parameter database for urban street canyon design.

Notwithstanding certain limitations, this study provides significant insights into diurnal and seasonal variations of airflow and thermal processes in urban street canyons.

**Author Contributions:** Conceptualization, Z.T.; Methodology, J.T. and Z.T.; Software, J.W., J.T. and Z.T.; Validation, Y.M.; Formal Analysis, J.W. and J.T.; Investigation, Y.M.; Data Curation, J.W.; Writing—original draft, J.W.; Writing—Review and Editing, Z.T.; Visualization, Y.M.; Supervision, Z.T.; Project administration, Z.T.; Funding Acquisition, Z.T. All authors have read and agreed to the published version of the manuscript.

**Funding:** This research was funded by the National Natural Science Foundation of China grant number [52008025] and Postdoctoral Research Foundation of China grant number [2021M700530]. And The APC was funded by [Chang'an University].

**Data Availability Statement:** The data presented in this study are available on request from the corresponding author.

**Conflicts of Interest:** The authors declare that they have no known competing financial interests or personal relationships that could have appeared to influence the work reported in this paper.

# Appendix A

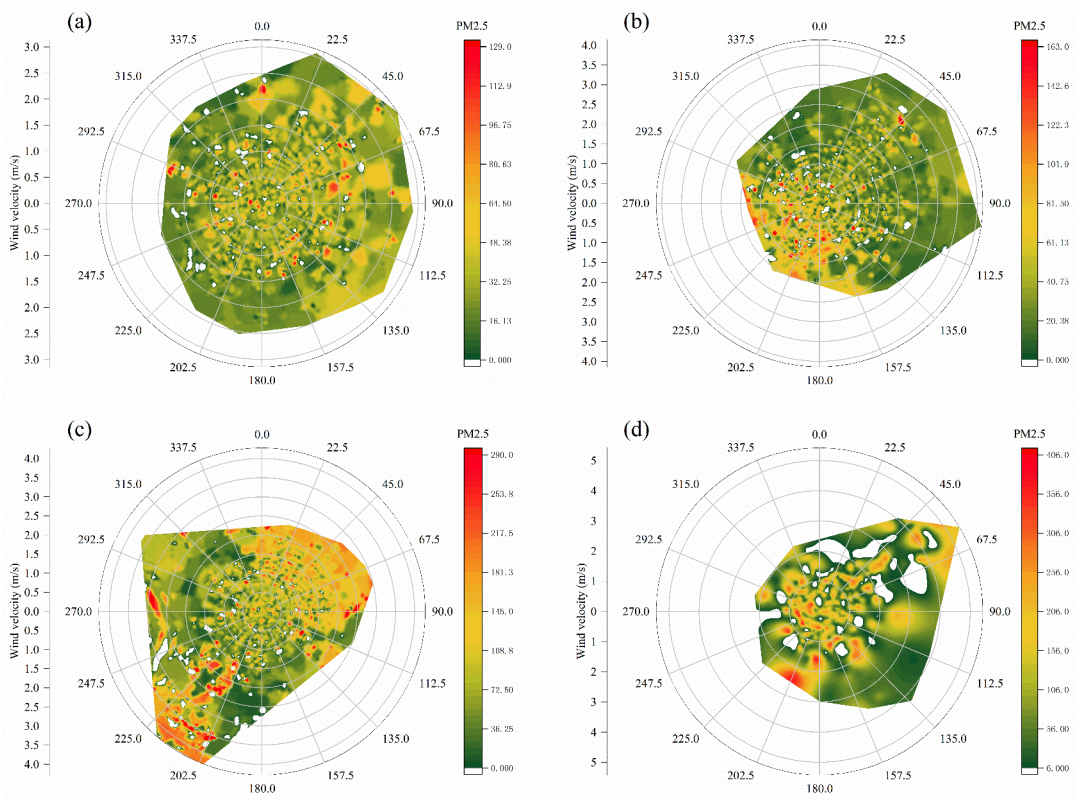


**Figure A1.** Radar rendering of seasonal wind velocity, direction, and pollutants in symmetric canyons: (**a**) winter; (**b**) spring; (**c**) summer; (**d**) autumn.

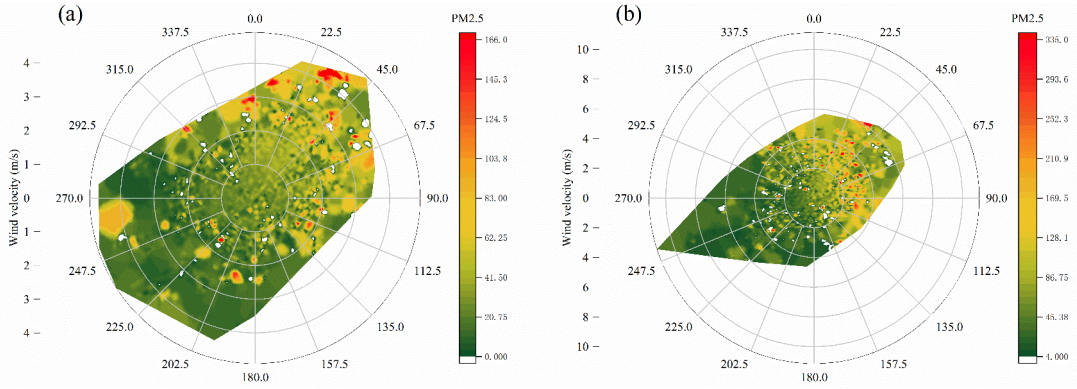


**Figure A2.** Radar rendering of wind velocity, direction, and pollutants in asymmetric canyons: (**a**) winter; (**b**) summer.

https://doi.org/10.3390/buildings16112134

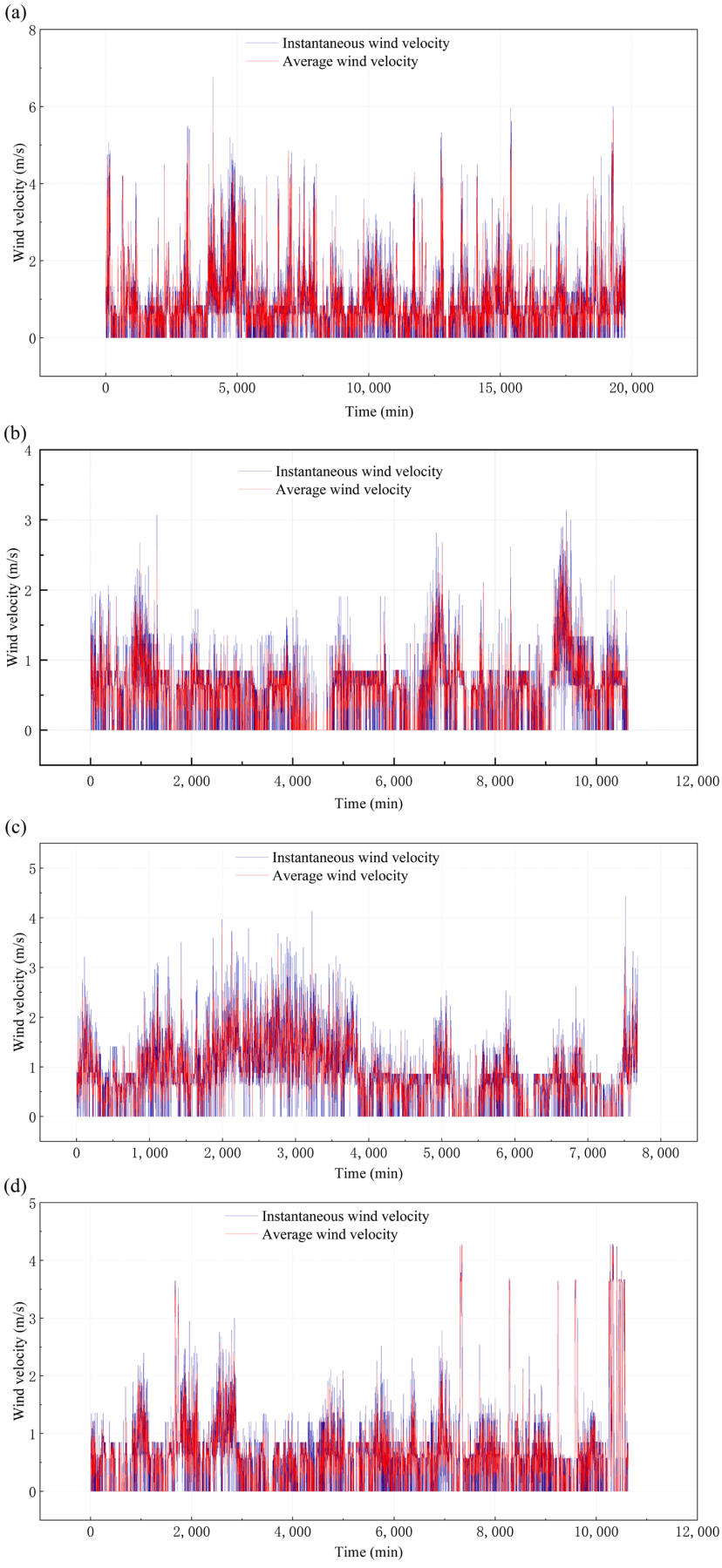


**Figure A3.** Symmetric street canyon measured average wind velocity and instantaneous wind velocity: (**a**) in winter; (**b**) in spring; (**c**) in summer; (**d**) in autumn.

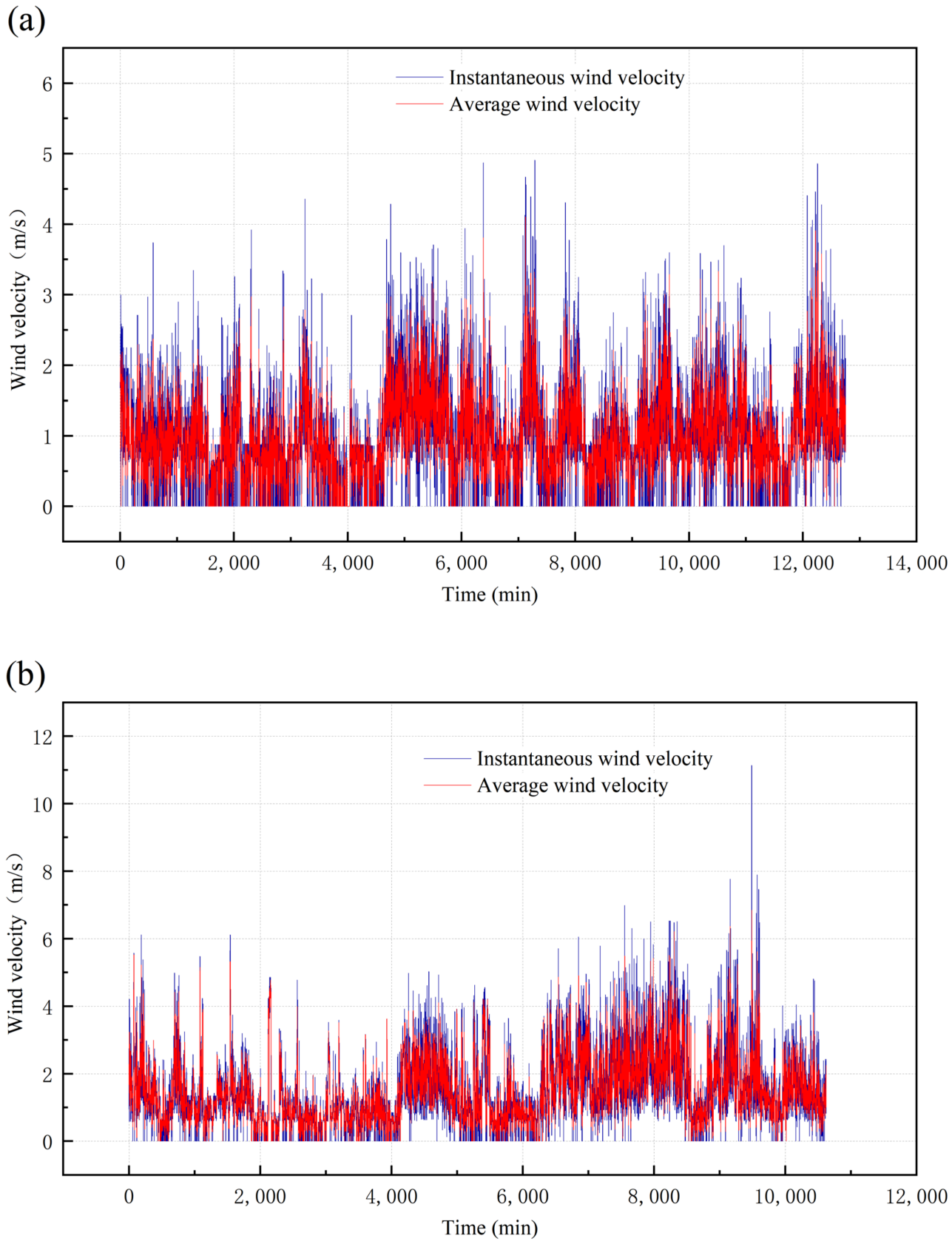


**Figure A4.** Asymmetric street canyon measured average wind velocity and instantaneous wind velocity: (**a**) in summer; (**b**) in winter.

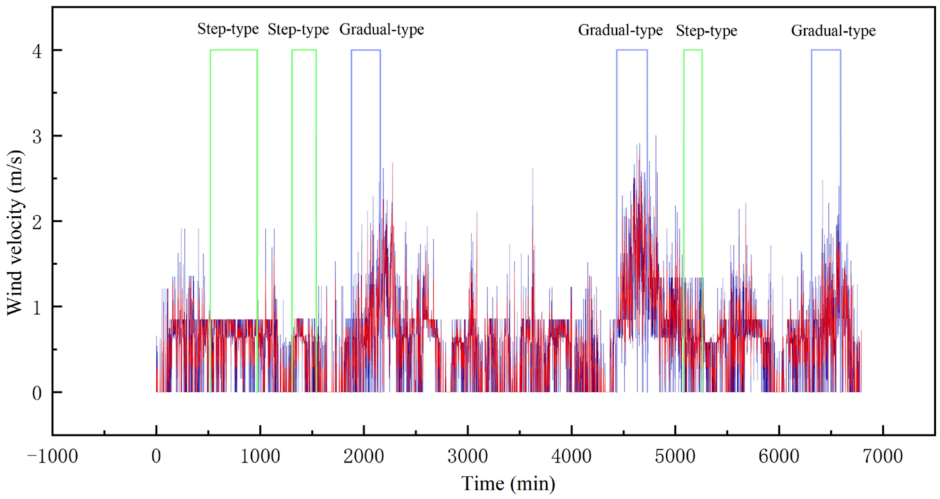


**Figure A5.** Step and gradient gust modes.

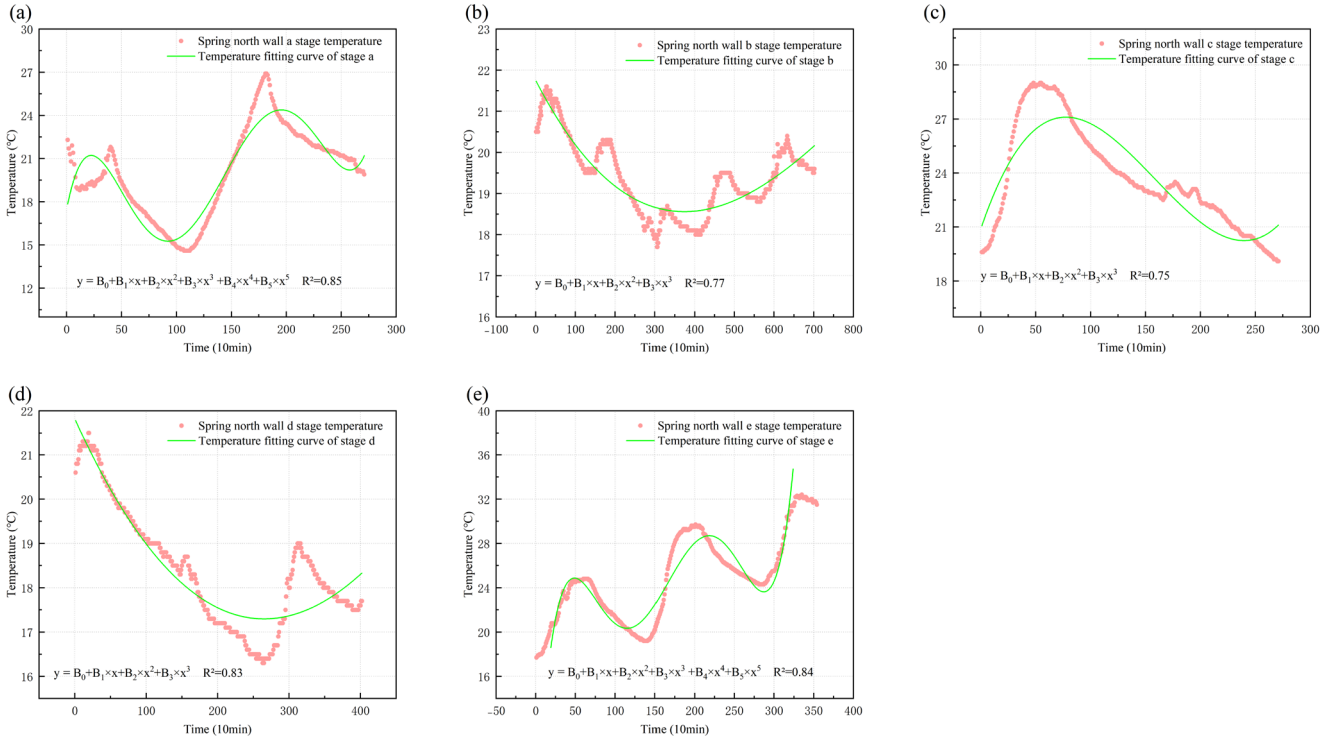


**Figure A6.** Symmetric street canyon spring north wall surface temperature fitting curves for phases (**a**–**e**).

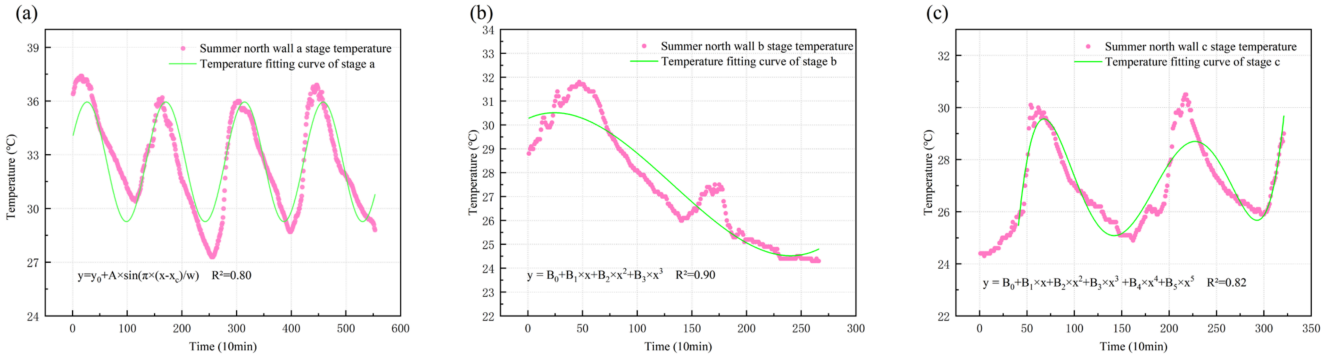


**Figure A7.** Symmetric street canyon summer north wall surface temperature fitting curves for phases (**a**–**c**).

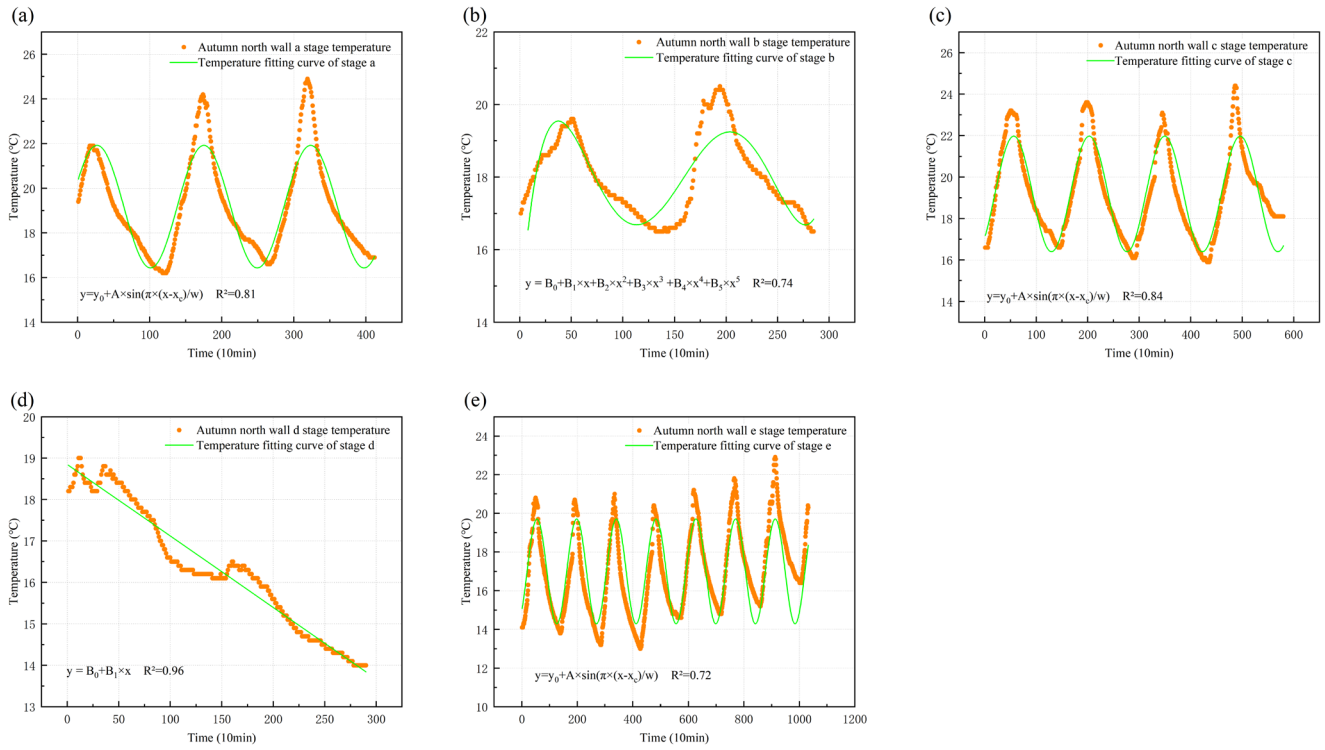


**Figure A8.** Symmetric street canyon autumn north wall surface temperature fitting curves for phases (**a**–**e**).

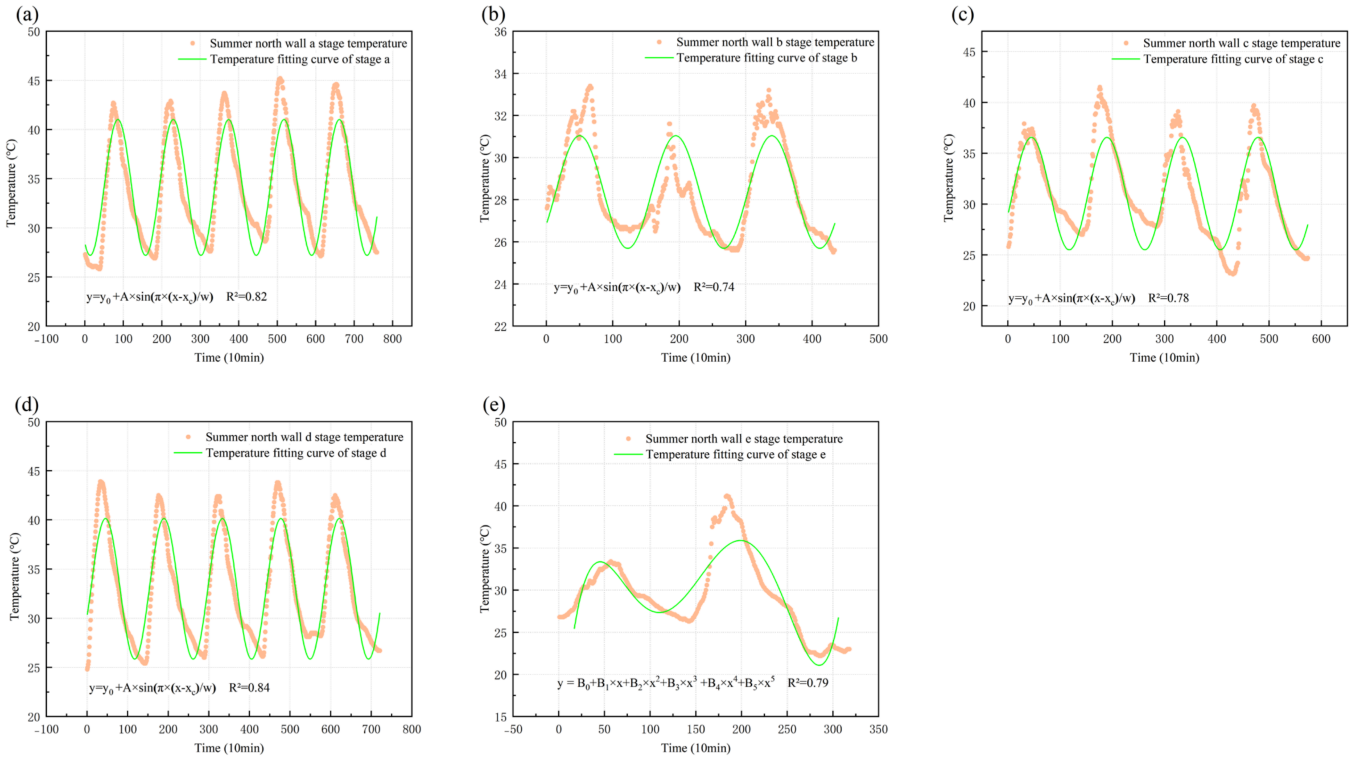


**Figure A9.** Asymmetric street canyon summer north wall surface temperature fitting curves for phases (**a**–**e**).

## References

1. Acar, H.; Yavuz, A.; Eroglu, E.; Acar, C.; Sancar, C.; Degermenci, A.S. Analysis of activity, space and user relations in urban squares. *Indoor Built Environ.* **2021**, *30*, 1466–1485. [CrossRef]

2. Borna, M.; Turci, G.; Marchetti, M.; Schiano-Phan, R. Evaluating the Influence of Urban Blocks on Air Pollution Concentration Levels: The Case Study of Golden Lane Estate in London. *Sustainability* **2024**, *16*, 696. [CrossRef]
3. Oke, T.R. Canyon geometry and the nocturnal urban heat island: Comparison of scale model and field observations. *J. Climatol.* **1981**, *1*, 237–254. [CrossRef]
4. Offerle, B.; Eliasson, I.; Grimmond, C.S.B.; Holmer, B. Surface heating in relation to air temperature, wind and turbulence in an urban street canyon. *Bound.-Layer Meteor.* **2007**, *122*, 273–292. [CrossRef]
5. Vranckx, S.; Vos, P.; Maiheu, B.; Janssen, S. Impact of trees on pollutant dispersion in street canyons: A numerical study of the annual average effects in Antwerp, Belgium. *Sci. Total Environ.* **2015**, *532*, 474–483. [CrossRef] [PubMed]
6. Wang, C.; Wang, Z.-H.; Ryu, Y.-H. A single-layer urban canopy model with transmissive radiation exchange between trees and street canyons. *Build. Environ.* **2021**, *191*, 107593. [CrossRef]
7. Du, H.; Savory, E.; Perret, L. Effect of morphology and an upstream tall building on the mean turbulence statistics of a street canyon flow. *Build. Environ.* **2023**, *241*, 110428. [CrossRef]
8. Segura, R.; Krayenhoff, E.S.; Martilli, A.; Badia, A.; Estruch, C.; Ventura, S.; Villalba, G. How do street trees affect urban temperatures and radiation exchange? Observations and numerical evaluation in a highly compact city. *Urban Clim.* **2022**, *46*, 101288. [CrossRef]
9. Ali-Toudert, F.; Mayer, H. Numerical study on the effects of aspect ratio and orientation of an urban street canyon on outdoor thermal comfort in hot and dry climate. *Build. Environ.* **2006**, *41*, 94–108. [CrossRef]
10. Feteha, S.; ElDeeb, S. Investigating urban canyons, façade albedo, and pedestrian thermal comfort using microclimate model calculations. *Build. Serv. Eng. Res. Technol.* **2024**, *45*, 457–473. [CrossRef]
11. Abdelmejeed, A.Y.; Gruehn, D. Optimizing an efficient urban tree strategy to improve microclimate conditions while considering water scarcity: A case study of Cairo. *Discov. Sustain.* **2024**, *66*, 36–66. [CrossRef]
12. Lv, W.; Wu, Y.; Zang, J. A Review on the Dispersion and Distribution Characteristics of Pollutants in Street Canyons and Improvement Measures. *Energies* **2021**, *14*, 6155. [CrossRef]
13. Klein, P.M.; Galvez, J.M. Flow and turbulence characteristics in a suburban street canyon. *Environ. Fluid Mech.* **2015**, *15*, 419–438. [CrossRef]
14. Zhang, Y.; Xu, W.; Wang, Q.; Su, J.; Huang, Y.; Gu, Z. Simulation on diurnal variation of thermal unsteady flow in a north—South orientated street canyon. *J. Earth Environ.* **2021**, *12*, 322–332.
15. Liu, B.; Liu, Y.; Cho, S.G.; Chow, D.H.C. Urban morphology indicators and solar radiation acquisition: 2011–2022 review. *Renew. Sust. Energ. Rev.* **2024**, *199*, 114548. [CrossRef]
16. Mei, D.; Wang, Y.; Deng, Q. Modeling the Airflow and Particle Dispersion in Street Canyons under Unsteady Thermal Environment with Sinusoidal Variation. *Aerosol Air Qual. Res.* **2017**, *17*, 1021–1032. [CrossRef]
17. Xiang, S.; Zhou, J.; Fu, X.; Zheng, L.; Wang, Y.; Zhang, Y.; Yi, K.; Liu, J.; Ma, J.; Tao, S. Fast simulation of high resolution urban wind fields at city scale. *Urban Clim.* **2021**, *39*, 100941. [CrossRef]
18. Donthu, E.V.S.K.K.; Kyriakodis, G.-E.; Zhang, X.; Long, Y.P.; Wan, M.P.; Bozonnet, E. Simulation advances with EnviBatE–A case study on urban heat island mitigation in Singapore. *Build. Environ.* **2024**, *258*, 111580. [CrossRef]
19. Zhang, Y.; He, S.; Gu, Z.; Wei, N.; Wah Yu, C.; Li, X.; Zhang, R.; Sun, X.; Zhou, D. Measurement, normalisation and mapping of urban-scale wind environment in Xi'an, China. *Indoor Built Environ.* **2018**, *28*, 1171–1180. [CrossRef]
20. Chai, M.-X.; Jon, K.S.; Sin, C.H.; Cui, P.-Y.; Luo, Y.; Huang, Y.-D. Effect of different canyon lengths and wind conditions on ventilation and pollutant dispersion inside asymmetric street canyons. *Environ. Fluid Mech.* **2025**, *25*, 24. [CrossRef]
21. Hersbach, H.; Bell, B.; Berrisford, P.; Biavati, G.; Horányi, A.; Muñoz Sabater, J.; Nicolas, J.; Peubey, C.; Radu, R.; Rozum, I.; et al. ERA5 Hourly Data on Single Levels from 1959 to Present. Copernicus Climate Change Service (C3S) Climate Data Store (CDS). 2018. Available online: www.xihe-energy.com (accessed on 12 December 2024).
22. *GB/T 21987-2017*; Grade of Cold Wave. Standards Press of China: Beijing, China, 2017.


**Disclaimer/Publisher's Note:** The statements, opinions and data contained in all publications are solely those of the individual author(s) and contributor(s) and not of MDPI and/or the editor(s). MDPI and/or the editor(s) disclaim responsibility for any injury to people or property resulting from any ideas, methods, instructions or products referred to in the content.